Int. J. Electrochem. Sci., 11 **(2016)** 1434 - 1455

International Journal of
ELECTROCHEMICAL
SCIENCE
www.electrochemsci.org

Characterization of Triazinedithiolsilane Polymeric Nanofilm Fabricated by Galvanostatic Technique on Copper surface

Zhong Liu and Yabin Wang[*]

Qinghai Institute of Salt Lakes, Chinese Academy of Sciences, Xining, Qinghai 810008, P. R. China
[*]E-mail: ybw@isl.ac.cn

Received: 13 November 2015 / *Accepted:* 14 December 2015 / *Published:* 1 January 2016

The polymeric nanofilm of a triazinedithiolsilane monosodium salt (abbreviated as TESPA) has been prepared by electrochemical technique and the following hydrolysis-condensation approach. The chemical composition and the morphology of the TESPA polymeric nanofilm were characterized by X-ray photoelectron spectroscopy (XPS) as well as energy-dispersive spectroscopy (EDS), and scanning electron microscope- (SEM), respectively. The XPS results reveal that: (1) Some dithiol groups from TESPA monomers electrochemically bond to copper surface and others polymerize to develop the polymeric structure of the disulfide units. These preferentially developed disulfide units protect the copper during the whole preparation process. (2) As the polymeric nanofilm is hydrolyzed, the obtained silanol groups could condense with each other to yield the siloxane networks along with the residual silanol groups under vacuum at high temperature. The SEM-EDS results demonstrate that the copper surfaces are uniformly covered with the polymeric nanofilms. New interface phases shape when the polymeric nanofilms are hydrolyzed with/without heating, which possess the multifunctionality of resisting corrosion and activating copper surface simultaneously.

Keywords: Copper; Galvanostatic technique; Scanning electron microscope; X-ray photoelectron spectroscopy

1. INTRODUCTION

According to the recently proposed design route of protecting metals against corrosion in our previous study [1], i.e., assembling two or more categories of protective groups to synthesize brand-new compounds and then fabricating the corresponding resistance structure from these novel compounds using various techniques, a type of triazinedithiolsilane compounds capable of resisting copper corrosion has been conceived and successfully synthesized by combining triazinedithiol and silane groups. 6-(3-triethoxysilylpropyl) amino-1, 3, 5-triazine-2, 4-dithiol monosodium salt

(abbreviated as TESPA) is one representative of such triazinedithiolsilane compounds. One kind of TESPA Polymeric nanofilm has been fabricated by self-assembled technique and the following heating. The results show that the polymeric nanofilm significantly inhibits copper corrosion; the formations of three-dimensional polymeric disulfide units (-SS-) and siloxane networks (SiOSi) account for the protective ability [2].

On the basis of the latter part of the design route (that is, fabricating the corresponding resistance structure from these novel compounds using various techniques), we fabricated another type of the TESPA polymeric nanofilm by electrochemical technique and the following hydrolysis-condensation approach according to scheme 1. It is the objective of this study to understand the chemical reactions between TESPA monomer and copper substrate, and unravel the component changes during the process of preparing the polymeric nanofilm by X-ray photoelectron spectroscopy (XPS) and energy-dispersive spectroscopy (EDS). Furthermore, the morphological characteristics of TESPA polymeric nanofilm on copper surfaces were also performed by means of scanning electron microscope (SEM).

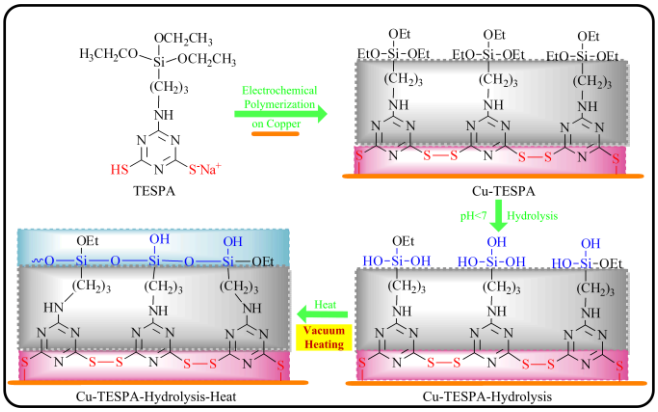

Scheme 1 Fabricating the TESPA polymeric nanofilm via electrochemical and the following hydrolysis-condensation approaches.

2. EXPERIMENTAL

2.1. Materials and reagents

6-(3-triethoxysilylpropyl)amino-1,3,5-triazine-2,4-dithiol monosodium salt was synthesized by reacting 6-(3-triethoxysilylpropylamino)-1,3,5-triazine-2,4-dichloride with NaSH according to our earlier study. Distilled water was used as solvent and Na_2CO_3 as supporting electrolyte. The concentrations of TESPA and supporting electrolytes were kept constant at 5 mM and 0.15 M, respectively. All of the chemicals were employed as analytical reagent (AR) without further purification. Test specimens (50 mm × 30 mm × 0.1 mm) of pure copper were abraded with emery paper of 1000 grit and 800 grit, and followed by fine polishing with alumina paste of 0.35 mm, 0.2 mm, 0.1mm particle size to achieve a mirror finish. The samples then degreased with acetone and

alcohol in an ultrasonic bath for 15 min, rinsed with copious distilled water, and finally dried by cold air from a hair dryer.

2.2. Fabricating TESPA polymeric nanofilm by galvanostatic technique

The electrochemical polymerization of TESPA was performed by using IM6ex workstation (Zahner, German) in a standard three-electrode system at room temperature. The electrolytic cell was equipped with working electrode (copper), Pt counter electrode (2 cm^2), and reference electrode (saturated calomel electrode, SCE). All potential values were referred to E_{SCE}. The cell was filled with electrolytic solution containing TESPA or not. In order to fabricate a more compact and uniform polymeric nanofilm, galvanostatic technique was carried out on copper substrates with a current density of 0.05 mA/cm^2 in TESPA-free and TESPA-contating Na_2CO_3 solutions at ambient temperature for 20 min. The as-deposited Cu-TESPA was hydrolyzed in a 0.1 M acetic acid (CH_3COOH) solution at 25°C for 30 min to yield Cu-TESPA-Hydrolysis surface. The obtained hydrolyzed surface was heated at 90°C for 15 min under vacuum to produce Cu-TESPA-Hydrolysis-Heat substrate. The aim of using vacuum curing is to eliminate the effect of copper oxide obtained from atmosphere heating. Herein, a bare copper reference was defined as Cu-Bare, and an electrochemically prepared sample as Cu-TESPA. The hydrolyzed Cu-TESPA without and with heating were recorded as Cu-TESPA-Hydrolysis and Cu-TESPA-Hydrolysis-Heat, respectively.

2.3. X-ray photoelectron spectroscopy (XPS)

XPS experiments were carried out on a ESCALAB 250Xi (Thermo Fisher Scientific) with Al Ka radiation ($h\upsilon$ = 1486.6 eV; analysed area= 600 μm^2). Unless specified otherwise, the X-ray anode was run at 250 W and the high voltage was kept at 15.0 kV with a detection angle of 45°. The base pressure of the analyzer chamber was around 5×10^{-8} Pa. A survey scan (0 ~ 1300 eV) was taken for all the samples in order to detect the present elements. Individual elemental scans of all the elements were then recorded with a comparative high resolution. The binding energy scale was calibrated from the hydrocarbon contamination using the C1s peak at 284.8 eV. It should be noted that all the binding energies from the references were re-calibrated using the C1s peak with the binding energy of 284.8 eV, to clearly understand the changes of the chemical states for the analysis of the peaks in our paper. For example, Cazorla-Amoro et. al [3] set the C1s peak position at 284.6 eV as the referential one using the Al Ka radiation; therefore, 0.2 eV (284.8 eV − 284.6 eV) was just added to all the peaks in that paper. This processing enables the analysis reasonable.

The software of XPS Peak 4.1 was adopted to de-convolve the Cu2p, C1s, O1s, N1s, S2p, and Si2p peaks using the Shirley-type background [4]. The parameters bound up with each peak in the software were binding energy centre, full width at half maximum (FWHM), peak area, and the Gaussian-to-Lorentzian ratio. We kept a combination of 80% Gaussian-20% Lorentzian line shape [5, 6], and maintained the FWHM of the various components in a given spectrum as close as possible [7].

The quality of the curve fit was monitored by the determination of χ^2; the "best fit" was achieved to consist with chemical meaning of each element during the process of performing the curve fitting.

The fractional concentration of a particular element X (X%) was calculated with formula 1 by applying atomic sensitivity factors (ASF) [8]:

$$X\% = \frac{(I_x / S_x)}{\sum (I_n / S_n)} \times 100\% \qquad (1)$$

Where I_n and S_n are the integrated peak areas and the sensitivity factors, respectively. The subscripts, x and n, stand for the element studied.

2.4. Scanning electron microscopy (SEM)

SEM-EDS study was performed at JSM-5610LV/INCA (JEOL Ltd., Japan), using a high-resolution environmental scanning electron microscope equipped with an energy-dispersive X-ray spectrometer (EDAX, Japan). Energy dispersive spectroscopy of the each surface was carried out in random areas for five times to identify the existed elements and their contents, which can further confirm the uniform coverage of the nanofilms.

3. RESULTS AND DISCUSSION

3.1. Representative XPS survey spectra of TESPA powder and the investigated surfaces.

Fig. 1 compares representative spectra obtained from the referential surfaces (TESPA powder and bare copper heated copper), and the studied surfaces (TESPA-deposited copper surface by electrochemical technique, TESPA-deposited copper surface plus hydrolysis without/with subsequent heating under vacuum).

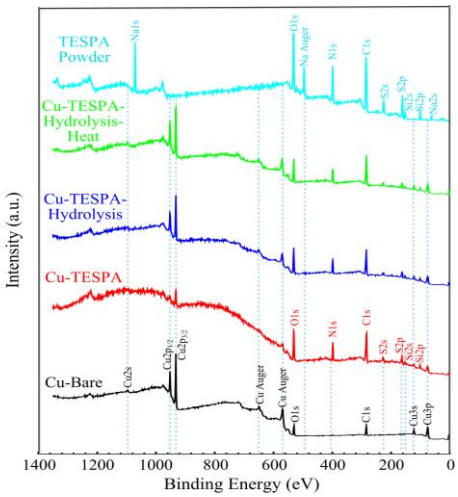

Figure 1. Representative XPS survey spectra from TESPA powder, as well as the surfaces of the bare copper, the TESPA-deposited copper, the hydrolyzed TESPA-deposited copper, and the hydrolyzed TESPA-deposited copper plus the following heating under vacuum.

Table 1. The present chemical elements and their corresponding atomic concentrations (AC, calculated by formula 1) of TESPA powder, as well as the surfaces of TESPA powder, the bare copper, the TESPA-deposited copper, the hydrolyzed TESPA-deposited copper, and the hydrolyzed TESPA-deposited copper plus the following heating under vacuum.

Sample	Na1s	Cu2p	C1s	O1s	N1s	S2p	Si2p
TESPA Powder	6.23	—	52.81	15.03	15.73	6.11	4.09
Cu-TESPA-Hydrolysis-Heat	—	9.81	54.51	14.13	14.28	4.27	2.99
Cu-TESPA-Hydrolysis	—	9.24	52.55	16.88	13.03	5.01	3.29
Cu- TESPA	—	2.66	54.22	19.03	15.02	5.18	3.88
Cu- Bare	—	25.39	51.89	22.72			

Table 1 shows the present chemical elements in each surface and the corresponding atomic concentrations. Because C1s and O1s coexist in all the five surfaces, thus the other elements are mainly analyzed and deciphered to reveal the chemical reactions between TESPA and copper.

It is intelligible that most samples exposed to the atmosphere will have a detectable quantity of adventitious carbon contamination commonly with a layer thickness of 1-2nm. C1s spectrum for contamination typically has three components: C-C, C-O-C and O-C=O [9], which accordingly gives rise to oxygen contamination of C-O-C and O-C=O [10]. Therefore, bare copper surface, which has been thoroughly cleaned and theoretically excludes carbon and oxygen elements, exhibits C1s and O1s spectra as expected. Na1s can be detectable in TESPA powder, but disappears for TESPA-deposited copper surfaces. The fundamental reason is that the S^- ions in SNa groups are electrochemically oxidized to SS units (see the following analyses of S2p XPS), and Na^+ ions dissolve in the electrolyte which can be removed during the cleaning procedure. The presence of N1s, S2s, S2p, Si2s and Si2p on all TESPA-deposited surfaces confirms that TESPA exists on the substrates (The reaction between TESPA and copper can be determined by the high-resolution XPS spectra of Cu2p3/2 and the Cu LMM Auger spectra in 3.3 below).

Although the numbers of N, S, and Si atoms in TESPA molecule are 4, 2, and 1 (see TESPA molecular structure in previous study), the practical specific values in Table 1 for TESPA powder, Cu-TESPA, Cu-TESPA-Hydrolysis, and Cu-TESPA-Hydrolysis-Heat surfaces are not exact 4:2:1. Two reasons account for this phenomenon. XPS is just a semi-quantitative analytical technique. On the other hand, S2s and Si2s are detectable in the survey scan, but their peak areas are not incorporated into the total areas of S and Si, because their high-resolution spectra cannot be given by individual elemental scans. Therefore, take sulphur for instance, the actual content merely comprises S2p excluding S2s; however, significant tendency can be seen. The atomic concentrations of N1s, S2p, and Si2p gradually decrease; the peak shapes of S2s and Si2s are smaller than that of S2p and Si2p, respectively. Compared with the XPS scan curves of the other four surfaces, the one of the Cu-TESPA is rough and abrupt from 600 eV to 1300 eV, which is the result of heterogeneous surface caused by electrochemical action.

3.2. The high-resolution XPS spectra of C1s and O1s for the investigated surfaces

Fig. 2 shows de-convolution of C1s for TESPA powder and the investigated surfaces. Relative chemical state, binding energy, FWHM and atomic concentration are reported in Table 2. As stated above, bare copper contains adventitious carbon contamination that can be resolved into C-C, C-O-C and O-C=O components. The types of carbon atoms in TESPA are comparatively larger and their chemical environments are relatively complicated. The de-convolution of the C1s spectrum of TESPA powder yields five types of carbon components as shown in Figure 2a. The peak at 284.20 eV can be attributed to the carbon bonded with silicon, because the electro-negativity of Si (1.74) is smaller than that of C (2.50) and H (2.10) according to Pauling Scale [11]. The electron density on this carbon is the largest; therefore, the binding energy has the lowest value. The electro-negativitis of other chemical elements involved in TESPA are as follows: N (3.07), S (2.44), and O (3.50). The peak centred at 284.80 eV is the calibrated carbon and the peak at 285.85 eV corresponds to C=N/C-S [12]. The higher peaks at 286.86 eV and 287.51 eV can be ascribed to C-N and C-O-Si [13, 14], respectively. It is obvious that we did not give peak of O-C=O for TESPA powder that emerge in the bare copper and TESPA-deposited surfaces, in view of numerous monomers in TESPA and neglectable amount of adventitious contamination. This analysis method of emphasizing the principal bulk runs through the whole study, when the core-level element is considered to be de-convoluted.

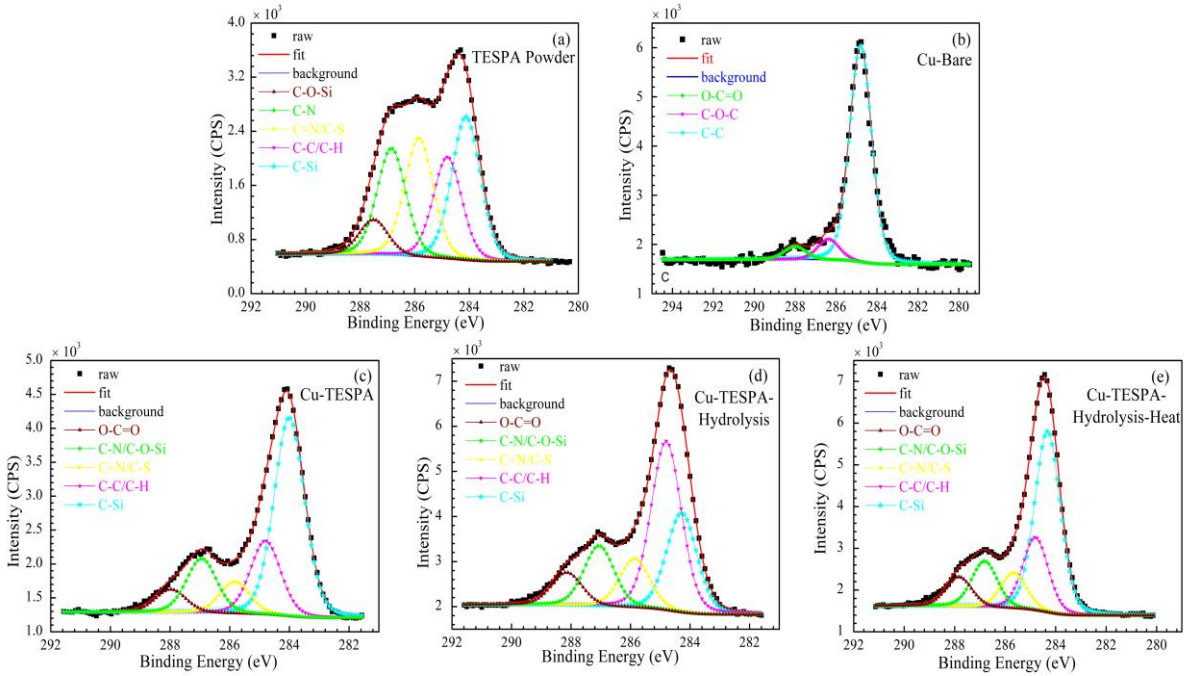

Figure 2. The high-resolution XPS spectra of C1s from TESPA powder, as well as the surfaces of the bare copper, the TESPA-deposited copper, the hydrolyzed TESPA-deposited copper, and the hydrolyzed TESPA-deposited copper plus the following heating under vacuum.

The de-convolution of the C1s spectra also produces five peaks for TESPA-electrodeposited copper surfaces; in contrast, obvious difference can be found between TESPA powder and the three. All in all, their peak shapes vary definitely and the peaks of TESPA-electrodeposited copper surfaces

resemble to a large extent. Detailed distinctions are as follows. First, the C1s peak of TESPA powder is drastically filled with sub-peaks of C-N, C-O-Si, C=N and C-S due to the existence of abundant TESPA monomers. The C1s peaks of TESPA-deposited copper surfaces become a little wizened in Figure 2c, 2d and 2e. Second, O-C=O peaks show up again on TESPA-treated copper surfaces at around 288.00 eV, because the amount of TESPA is nano-scale in the nanofilms. The TESPA monomers within the nanofilms turn out to be rare than that of TESPA powder; hence, the influence of adventitious carbon contamination cannot be neglected (Figure 2c, 2d and 2e).

Table 2. The present chemical states of C1s in TESPA powder, as well as the surfaces of the bare copper, the TESPA-deposited copper, the hydrolyzed TESPA-deposited copper, and the hydrolyzed TESPA-deposited copper plus the following heating under vacuum. The corresponding binding energy, full width at half maximum (FWHM) and atomic concentration (AC) of each chemical state are also given.

Sample	Chemical State	Binding Energy (eV)	Area	FWHM	AC (%)
TESPA Powder	C-Si	284.20	3062.94	1.24	28.36
	C-C/C-H	284.80	2173.33	1.24	20.12
	C=N/C-S	285.85	2538.32	1.24	23.50
	C-N	286.86	2284.50	1.24	21.15
	C-O-Si	287.51	741.77	1.24	6.87
Cu- Bare	C-C	284.80	6420.62	1.25	86.55
	C-O-C	286.37	612.06	1.25	8.25
	O-C=O	288.00	386.11	1.25	5.20
Cu-TESPA	C-Si	284.003	4096.92	1.20	52.14
	C-C/C-H	284.8	1519.06	1.20	19.33
	C=N/C-S	285.824	653.57	1.20	8.32
	C-N/ C-O-Si	286.941	1115.36	1.20	14.20
	O-C=O	287.978	471.94	1.20	6.01
Cu-TESPA-Hydrolysis	C-Si	284.278	3082.00	1.20	24.22
	C-C/C-H	284.8	5246.44	1.20	41.22
	C=N/C-S	285.861	1516.72	1.20	11.92
	C-N/ C-O-Si	287.057	1871.61	1.20	14.70
	O-C=O	288.143	1010.32	1.20	7.94
Cu-TESPA-Hydrolysis-Heat	C-Si	284.323	6071.85	1.20	49.58
	C-C/C-H	284.8	2447.24	1.20	19.98
	C=N/C-S	285.661	1198.24	1.20	9.79
	C-N/ C-O-Si	286.818	1543.77	1.20	12.61
	O-C=O	287.834	984.36	1.20	8.04

In sum, XPS is a technique for analyzing the surface chemistry of a material. Electrons emitted from the top 1~10 nm of the material can only be analyzed [15], therefore, the material bulk determines the splitting of the core-level peak. As is shown, the C1s peaks of TESPA powder and the

TESPA-containing surfaces were discriminatively de-convoluted according to the raw peak shapes and the peak positions.

Fig. 3 shows de-convolution of O1s for TESPA powder and the investigated surfaces.. Relative chemical state, binding energy, FWHM and atomic concentration are listed in Table 3. Bare copper possesses adventitious carbon contamination of C-C, C-O-C and O-C=O components. Accordingly, the C-O-C and O-C=O peaks of oxygen contamination from the reference are located at 532.47 eV and 531.55 eV (Figure 3b) [16, 17]. Besides, the lowest peaks at 530.55 eV for bare copper is copper oxide/cuprous oxide (CuO/Cu_2O) [18], which is commonly identified as chemical states of metal oxides [18, 19]. The existence of abundant TESPA monomers can eliminate the adventitious oxygen contamination for TESPA powder (Figure 3a); hence, the main peak is considered to be Si-O-C at 531.96 eV [20], excluding C-O-C and O-C=O. Whereas, a much broader peak at 535.28 eV with a higher FWHM of 2.23 than that of O1s component, can be assigned to sodium Auger peak (Na KLL) [21, 22] due to a considerable amount of Na^+ in TESPA. This result confirms the removal of Na^+ during the cleaning procedure when TESPA is electrochemically deposited on copper surface, consistent with the explanation for survey scan.

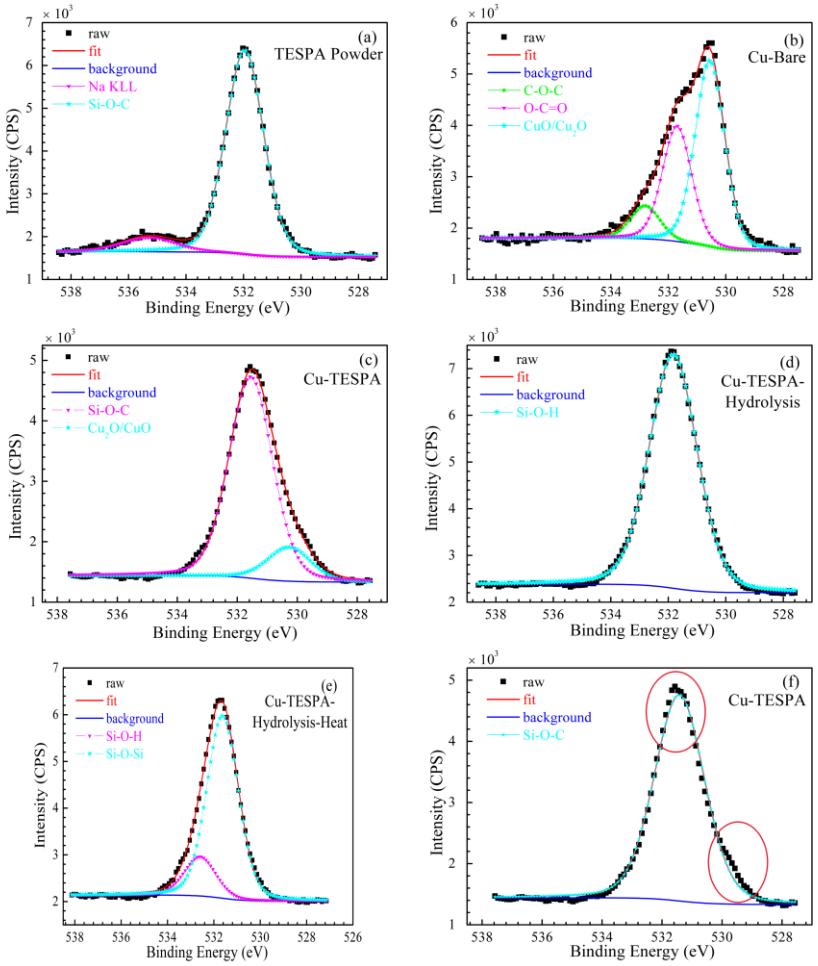

Figure 3. The high-resolution XPS spectra of O1s from TESPA powder, as well as the surfaces of the bare copper, the TESPA-deposited copper, the hydrolyzed TESPA-deposited copper, and the hydrolyzed TESPA-deposited copper plus the following heating under vacuum.

Table 3. The present chemical states of O1s in TESPA powder, as well as the surfaces of the bare copper, the TESPA-deposited copper, the hydrolyzed TESPA-deposited copper, and the hydrolyzed TESPA-deposited copper plus the following heating under vacuum. The corresponding binding energy, full width at half maximum (FWHM) and atomic concentration (AC) of each chemical state are also given.

Sample	Chemical State	Binding Energy (eV)	Area	FWHM	AC (%)
TESPA Powder	Si-O-C	531.96	8621.82	1.55	100.00
	Na KLL	535.28	850.86	2.23	—
Cu- Bare	CuO/Cu_2O	530.55	5065.49	1.20	55.58
	O-C=O	531.70	3146.73	1.20	34.52
	C-O-C	532.80	902.43	1.20	9.90
Cu-TESPA	CuO/Cu_2O	530.27	1119.60	1.70	14.49
	Si-O-C	531.55	6606.82	1.70	85.51
Cu-TESPA-Hydrolysis	Si-O-H	531.82	11467.29	1.96	100.00
Cu-TESPA-Hydrolysis -Heat	Si-O-Si	532. 60	1566.39	1.60	17.69
	Si-O-H	531.62	7288.18	1.60	82.31

As for Cu-TESPA (Fig. 3c), two signals are decomposed of oxygen. Peak at 530.27 eV can be attributed to Cu_2O/CuO which is caused by the oxidation of copper; peak centred at 531.55 eV is the signal of oxygen in $SiOCH_2CH_3$ groups. When Cu-TESPA surface is fully hydrolyzed under acetic acid, two classes of chemical reactions occur. One is the hydrolysis of triethoxysilyl groups, namely, the $SiOCH_2CH_3$ groups transform to SiOH groups; the other is acid-base reaction, i.e., Cu_2O and CuO located at the top of copper surface react with H^+. The latter chemical reaction gives rise to the disappearance of Cu_2O/CuO peaks for both Cu-TESPA-Hydrolysis (Figure 2d) and Cu-TESPA-Hydrolysis-Heat (Figure 2e) substrates. In order to clearly reveal this change, a comparison sample is exhibited in Fig. 2f where the peak of O1s in Cu-TESPA is not de-convoluted, and the bad fitting result can be easily observed in the pink circle.

Fully hydrolyzed Cu-TESPA owns one major chemical state of oxygen. The O1s peak is evidently symmetric, and can be ascribed to Si-O-H at 531.82 eV [23]. Although the O1s peak from hydrolyzed TESPA-deposited copper surface plus heating (Figure 3e) is also symmetric, it should be decomposed into two peaks of Si-O-H and Si-O-Si. Si-O-Si networks are introduced by heating the hydrolyzed Cu-TESPA in vacuum via dehydration of Si-O-H groups [23, 24], and the residual naturally lead to Si-O-H signal which is verified by contact angle test in part one as well. The FWHM of TESPA-containing copper surfaces are far from the references and nearly the same to the TESPA powder, indicating that the surfaces have been functioned with TESPA and contain a wide distribution [3].

3.3. The high-resolution XPS spectra of Cu2p$_{3/2}$ and the Cu LMM Auger spectra for the investigated surfaces

Any changes of peak shape and position, observed in the XPS spectra from the referential and investigated surfaces, must be the result of specific interactions between TESPA and copper. In order to understand the chemical reactions between copper and TESPA, the changes of Cu2p from the studied surfaces are compared in Figure 4. For the TESPA treated surfaces and the references, typical Cu2p$_{3/2}$ and Cu2p$_{1/2}$ can be observed that has significantly split spin-orbit components (Δ_{metal}=19.75eV) [25]. Both the bare copper and the TESPA-deposited surfaces exhibit the Cu(II) satellite peaks which come from copper oxide (CuO) [25, 26]. The satellite peak of Cu-TESPA is more apparent because plenty of copper oxides can be produced by electrochemical action.

When copper surface is hydrolyzed, the satellite peak vanishes certifying the dissolution of CuO in acetic acid. Subsequently, this surface is cured under vacuum environment at high temperature, and the satellite peak does not appear. Here, an assumption can be put forward that even the Cu-TESPA-Hydrolysis is heated under atmosphere with the same conditions, the surface will not be oxidized. Since we have found that even TESPA SAM was cured under atmospheric environment at high temperature, the satellite peak does not emerge due to the outstanding protective capability of triazinedithiolsilane compounds.

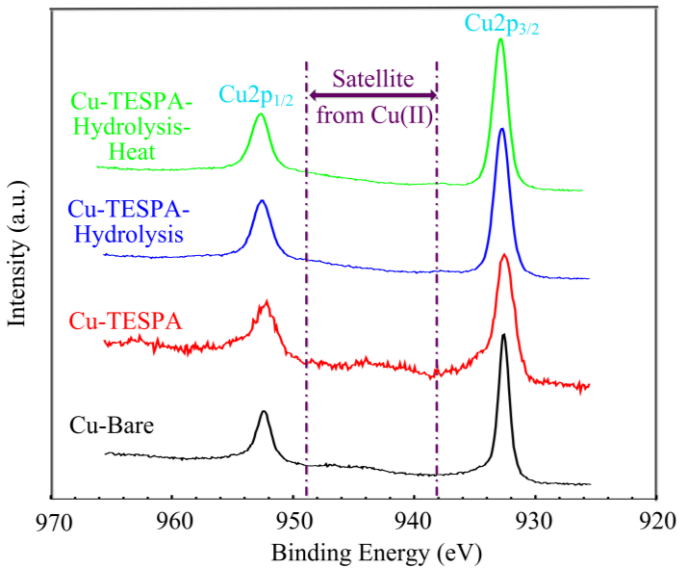

Figure 4. Representative XPS survey spectra of Cu2p from the surfaces of the bare copper, the TESPA-deposited copper, the hydrolyzed TESPA-deposited copper, and the hydrolyzed TESPA-deposited copper plus the following heating under vacuum.

To further identify the protective effect, Cu2p$_{3/2}$ peaks are investigated in Fig. 5. Relative chemical state, binding energy, FWHM and atomic concentration are presented in Table 4. The shapes of Cu2p$_{3/2}$ peaks from the bare and TESPA-deposited surfaces are asymmetric, while the other two are symmetric that cannot be split. The bare and TESPA-deposited surfaces are resolved into two peaks,

corresponding to Cu(0)/Cu(I), and Cu(II) (Figure 5a and 5b) [27]. The hydrolyzed and heated surfaces are not split, only including Cu(0)/Cu(I) (Figure 5c and 5d).

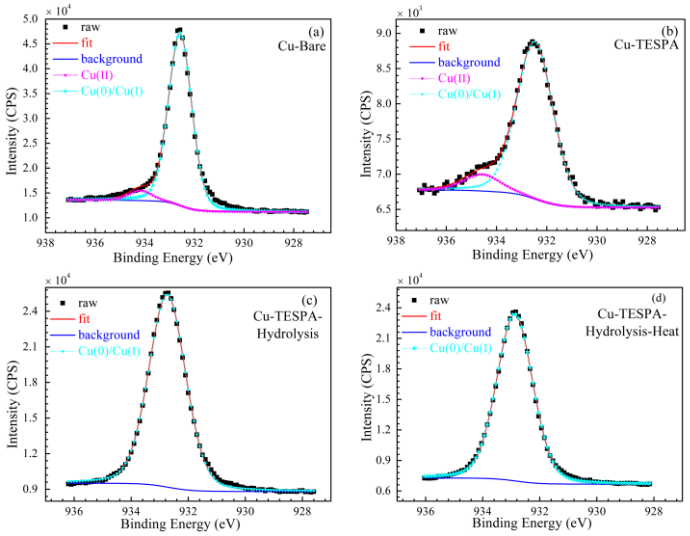

Figure 5. The high-resolution XPS spectra of $Cu2p_{3/2}$ from the surfaces of the bare copper, the TESPA-deposited copper, the hydrolyzed TESPA-deposited copper, and the hydrolyzed TESPA-deposited copper plus the following heating under vacuum.

From the hydrolyzed and heated surfaces, it can be concluded that Cu(II)S/Cu(II)O species do not exist on their surfaces. That is, SH groups participate in two kinds of chemical reactions with copper: reduction reaction of CuO to Cu(0) or Cu(I)O, and chemical adsorption with copper to yield Cu(I)S.

Table 4. The present chemical states of $Cu2p_{3/2}$ in the surfaces of the bare copper, the TESPA-deposited copper, the hydrolyzed TESPA-deposited copper, and the hydrolyzed TESPA-deposited copper plus the following heating under vacuum. The corresponding binding energy, full width at half maximum (FWHM) and atomic concentration (AC) of each chemical state are also given.

Sample	Chemical State	Binding Energy (eV)	Area	FWHM	AC (%)
Cu- Bare	Cu(0)/Cu(I)O	932.58	44623.09	1.10	94.53
	Cu(II)O	934.17	2583.04	1.10	5.47
Cu-TESPA	Cu(0)/Cu(I)O	932.47	4437.17	1.70	90.45
	Cu(II)O/ Cu(II)-CO_3^{2-}	934.58	468.39	1.70	9.55
Cu-TESPA-Hydrolysis	Cu(0)/Cu(I)	932.74	28797.68	1.52	100.00
Cu-TESPA-Hydrolysis -Heat	Cu(0)/Cu(I)	932.87	28421.75	1.49	100.00

Cu(I) can be absolutely verified by the changes of Cu LMM on the four surfaces in Fig. 6. The centres of the Cu LMM peak for Cu_2O, CuO, and copper metal locate at 570.6 eV, 569.0 eV, and 568.2 eV, respectively, identical to reports in literature [28, 29]. A forth component of the Cu LMM spectra is located at 571.5 eV for the cleaned TESPA-deposited copper surfaces. This component is attributed to the formation of the Cu(I), which is similar to [Cu(I)BTA] complex previously observed at 571.8 eV [30]. It should be pointed that Cu(I) is complicated, because Cu(I)N compound may be yielded between TESPA and copper as TESPA SAM does, apart from Cu(I)S compound. To identify the existence of Cu(I)N compound, the high-resolution XPS spectra of N1s will be discussed later. Compared with the representative XPS survey spectra of Cu LMM from self-assembled investigation, a distinction can be seen. The intensity of Cu LMM from Cu-TESPA is the lowest, and the signal is not that apparent. This phenomenon can be explained as follows. When copper is electrochemically oxidized, Cu(0)/Cu(I) complexes yield, cover the substrate surface, and block the electrons from X-ray. As the surface is immersed in acetic acid and washed by de-ionized water, these electrochemical products are resolved and the surface becomes clean again, giving rise to the strong signals of the substrates. The self-assembled process is free of electrochemically induced contaminants formed atop the studied surfaces.

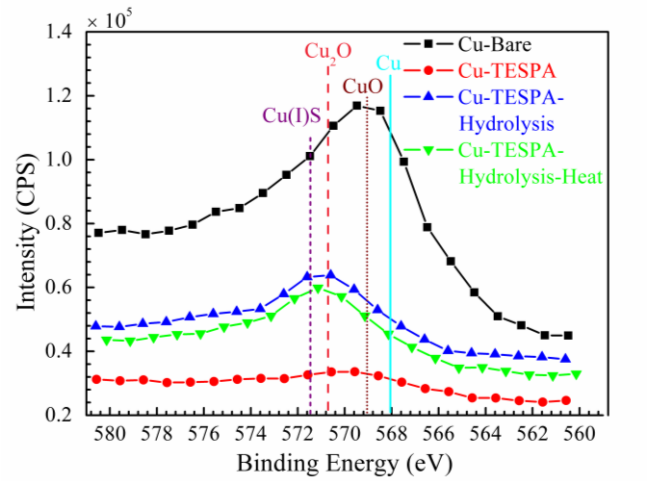

Figure 6. Representative XPS survey spectra of Cu LMM from the surfaces of the bare copper, the TESPA-deposited copper, the hydrolyzed TESPA-deposited copper, and the hydrolyzed TESPA-deposited copper plus the following heating under vacuum.

3.4. The high-resolution XPS spectra of S2p, N1s and Si2p for the TESPA-containing surfaces

On the basis of the $Cu2p_{3/2}$ and Cu LMM spectra, it is clear that Cu(I)S compound have formed on copper surface. But the polymerization of -SH groups has not been verified, hence S2p spectra are investigated in Fig. 7 for the TESPA-deposited surfaces. All the S2p peaks were fit using one doublet with a splitting of 1.2 eV and a 2:1 area ratio [31]. Chemical state, relative binding energy, FWHM and atomic concentration are shown in Table 5.

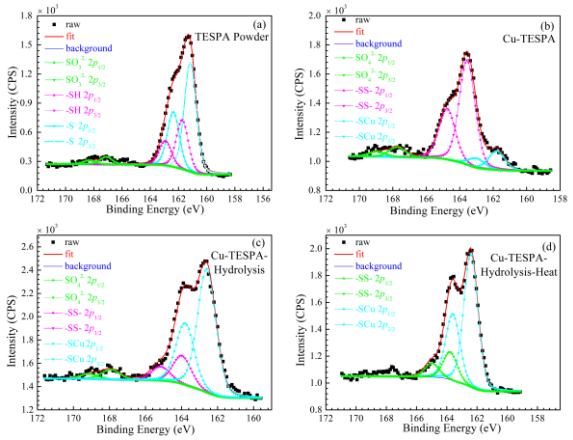

Figure 7. The high-resolution XPS spectra of S2p from TESPA powder, as well as the surfaces of the TESPA-deposited copper, the hydrolyzed TESPA-deposited copper, and the hydrolyzed TESPA-deposited copper plus the following heating under vacuum.

Table 5. The present chemical states of S2p in TESPA powder, the TESPA-deposited copper surface, the hydrolyzed TESPA-deposited copper surface, and the hydrolyzed TESPA-deposited copper surface plus the following heating under vacuum. The corresponding binding energy, full width at half maximum (FWHM) and atomic concentration (AC) of each chemical state are also given.

Sample	Chemical State	Binding Energy (eV)	Area	FWHM	AC (%)
TESPA Powder	$S^{-}2p_{3/2}$	161.16	1319.94	1.00	43.93
	$S^{-}2p_{1/2}$	162.36	659.97	1.00	21.97
	$SH2p_{3/2}$	161.73	590.80	1.00	19.67
	$SH2p_{1/2}$	162.93	295.40	1.00	9.83
	$SO_3^{2-}2p_{3/2}$	167.12	92.09	1.00	3.07
	$SO_3^{2-}2p_{1/2}$	168.32	46.04	1.00	1.53
Cu-TESPA	$SCu2p_{3/2}$	161.78	174.23	1.15	9.65
	$SCu2p_{1/2}$	162.98	87.11	1.15	4.83
	$SS2p_{3/2}$	163.56	936.65	1.12	51.89
	$SS2p_{1/2}$	164.76	468.33	1.15	25.94
	$SO_4^{2-}2p_{3/2}$	167.74	92.55	1.15	5.13
	$SO_4^{2-}2p_{1/2}$	168.94	46.28	1.15	2.56
Cu-TESPA-Hydrolysis	$SCu2p_{3/2}$	162.60	1486.37	1.20	50.94
	$SCu2p_{1/2}$	163.80	743.19	1.20	25.47
	$SS2p_{3/2}$	163.97	338.90	1.20	11.61
	$SS2p_{1/2}$	165.17	169.45	1.20	5.81
	$SO_4^{2-}2p_{3/2}$	167.93	120.13	1.20	4.12
	$SO_4^{2-}2p_{1/2}$	169.13	60.07	1.20	2.06
Cu-TESPA-Hydrolysis-Heat	$SCu2p_{3/2}$	162.40	1273.06	1.10	55.22
	$SCu2p_{1/2}$	163.60	636.53	1.10	27.61
	$SS2p_{3/2}$	163.77	264.03	1.10	11.45
	$SS2p_{1/2}$	164.97	132.02	1.10	5.72

Six distinguishable peaks with three chemical states, located at 162.36 eV (161.16 eV), 162.93 eV (161.73 eV), and 168.32 eV (167.12 eV), are resolved for $S2p_{1/2}$ ($S2p_{3/2}$) in TESPA powder (Figure 7a). The lowest-energy state arises from S^- [32], because sulfer in this chemical environment has the most electron density. Peaks at 162.93 eV (161.73 eV) are assigned to dithiol groups in TESPA [33]. The highest chemical state can be assigned to SO_3^{2-} [34, 35] which has been oxidized because of X-ray during the process.

As TESPA monomers in Na_2CO_3 electrolyte have been electrochemically deposited on copper surface, three chemical states of S2p form. Sub-bands of 161.79 eV (162.99 eV) (Figure 7b) are ascribed to bound thiolate species of –SCu in Cu-TESPA [36, 37], because of the high affinity of SH group with copper. This result is in agreement with our interpretation of the effects from Cu LMM. The second type of peaks at 164.76 eV (163.56 eV) stand for polymerization of SH groups to disulfide units [31, 38, 39]. Another type of peaks at 168.94 eV (167.74 eV) are assigned to the sulfate radical (SO_4^{2-}) [35] caused by the oxidation of SH groups under electrochemical action. Cu-TESPA-Hydrolysis holds the same peaks like Cu-TESPA; however, the peak and their positions are more close to theoretical value due to the removal of by-products, such as Cu(II) complex. After heating Cu-TESPA-Hydrolysis in vacuum, no obvious difference can be seen, except peaks of contaminative SO_4^{2-} disappear. The results reveal that the bound chemical bonds and the resulting polymeric disulfide units with three dimensions protect copper simultaneously, suppressing the ingress of Cl- through the nanofilms.

N1s of the TESPA-containing surfaces are de-convoluted in Fig. 8. Chemical state, relative binding energy, FWHM and atomic concentration are shown in Table 6. A variety of studies have reported two chemical states of six nitrogen atoms in melamine resin [3, 40], owing to the symmetric structure where N1s (sp^3) locates at 399.6 and N1s (sp^2) centres at 398.9 (see Figure 9, structure 1). It is commonly acceptable that sp^2 hybrid possesses a higher electron density than sp^3 hybrid due to a larger percentage of *s* orbital; correspondingly, N1s (sp^2) has a lower binding energy than that of N1s (sp^3) similar to sp^2 and sp^3 of C1s where the former shifts to a lower binding energy [41]. TESPA monomer contains four nitrogen atoms that are asymmetrically distributed, and according to the chemical environment, we divide them to three chemical states (see Figure 9, structure 1, 2, and 3). N1s states in structure 1 and 2 are differentiated due to the adjacent various functional groups, namely, the-SH and -SNa groups which can be considered to replace the $–NH_2$ in melamine. For triazinedithiol monomers, electron densities of the aromatic rings are determined by conjugated effect and inductive effect [42, 43]. -NH- and -SH/SNa groups provide positive conjugated effect and negative inductive effect, but the former effect dominates [44, 45]. Besides, the electro-negativity of S is smaller than that of N. The above factors lead to a higher electron density of N1s in structure 1 than that of the N1s in structure 2. As a result, nitrogen atoms embedded in aromatic ring and close to the ex-ocyclic NH group have a lower binding energy.

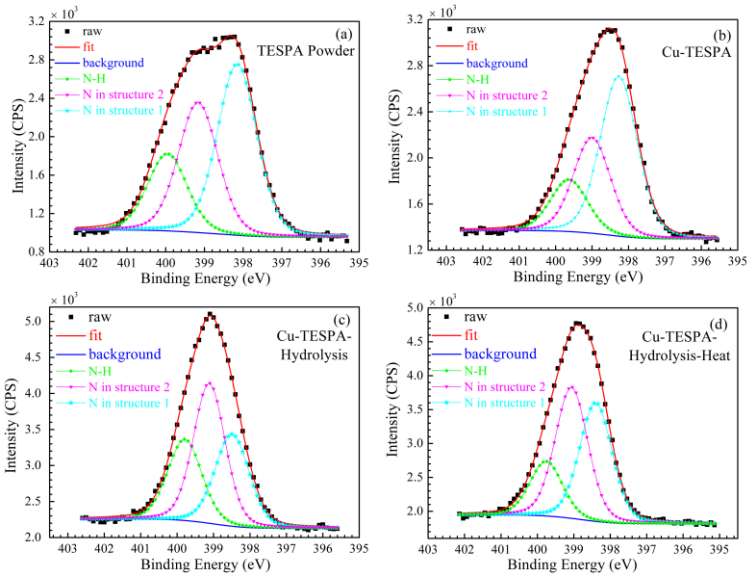

Figure 8. The high-resolution XPS spectra of N1s from TESPA powder, as well as the surfaces of the TESPA-deposited copper, the hydrolyzed TESPA-deposited copper, and the hydrolyzed TESPA-deposited copper plus the following heating under vacuum.

Table 6. The present chemical states of N1s in TESPA powder, the TESPA-deposited copper surface, the hydrolyzed TESPA-deposited copper surface, and the hydrolyzed TESPA-deposited copper surface plus the following heating under vacuum. The corresponding binding energy, full width at half maximum (FWHM) and atomic concentration (AC) of each chemical state are also given.

Sample	Chemical State (Structure in Fig. 9)	Binding Energy (eV)	Area	FWHM	AC (%)
TESPA Powder	N in structure 1 (sp^2)	398.16	2494.51	1.20	45.21
	N in structure 2 (sp^2)	399.16	1899.27	1.20	20.36
	N-H (sp^3)	399.96	1123.66	1.20	34.42
Cu-TESPA	N in structure 1 (sp^2)	398.27	1940.84	1.20	51.96
	N in structure 2 (sp^2)	399.00	1163.09	1.20	31.14
	N-H (sp^3)	399.63	631.31	1.20	16.90
Cu-TESPA-Hydrolysis	N in structure 1 (sp^2)	398.49	1640.79	1.10	30.30
	N in structure 2 (sp^2)	399.11	2326.84	1.10	42.98
	N-H (sp^3)	399.79	1446.74	1.03	26.72
Cu-TESPA-Hydrolysis-Heat	N in structure 1 (sp^2)	398.40	2140.88	1.05	38.90
	N in structure 2 (sp^2)	399.06	2374.86	1.05	43.15
	N-H (sp^3)	399.76	987.73	1.05	17.95

Actually, we have found a higher peak located at 400.25 ~ 400.63 eV when TESPA monomers self-assemble onto copper. The higher binding energy is a result of chemical reaction between nitrogen and copper; the former can easily donate the electron pair, and the latter can provide unoccupied molecular orbital. These natures accelerate the formation of a chemical bond between nitrogen and copper atoms, which reduces the electron density and boosts the binding energy towards a higher value

[46]. However, no such a higher peak is observed when TESPA monomers are electrochemically deposited on copper surface.

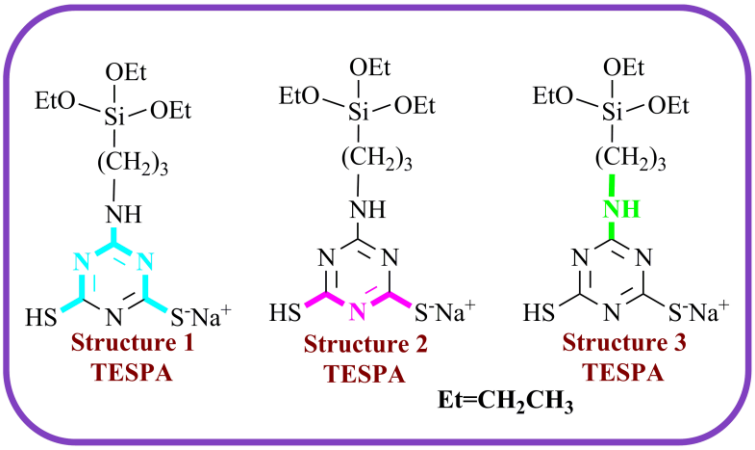

Figure 9. Chemical environments of N1s in TESPA molecule.

Although we have amply confirmed the formation of SiOSi networks via electrochemical impedance spectroscopy (EIS) and contact angle test (CA) in the first part; however, the transformation of Si chemical states is less know. Si2p of TESPA powder and TESPA-treated surfaces are shown in Figure 10. Given the symmetry and regularity of the raw peak, as well as the existence of numerous bulk monomers, silicon of TESPA is believed to have one chemical environment of -$Si(OCH_2CH_3)_3$ with the peak located at 101.62 eV (Figure 10) [47].

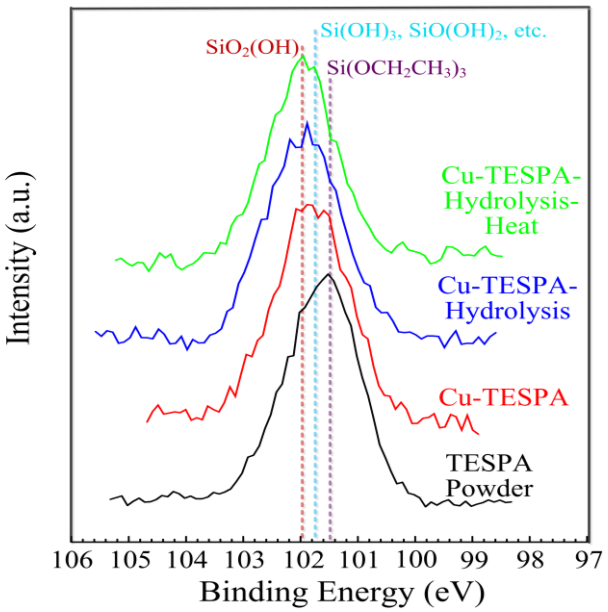

Figure 10. The high-resolution XPS spectra of Si2p from TESPA powder, as well as the surfaces of the TESPA-deposited copper, the hydrolyzed TESPA-deposited copper, and the hydrolyzed TESPA-deposited copper plus the following heating under vacuum.

As TESPA monomers are electrochemically deposited on copper surface, parts of them hydrolyze and transform into structures of intermediate products at higher positions, such as -$Si(OH)_3$ and -$SiO(OH)_2$, due to the aqueous solution and electrochemical deposition time sustained about twenty minutes. When the surface of Cu-TESPA is hydrolyzed, the peak shifts to a higher position indicating the formation of abundant intermediate products. These hydrolyzed products condense and lose water to give rise to the SiOSi networks with the structure of -$SiO_2(OH)$ at the highest position. The content of OH groups remarkably decrease and the residual OH groups determine the wettability ability of the surface, which is in agreement with the results of contact angle [48]. It should be noted that the Si2p peak position in this work extremely differ from the results of Gu et al. Un-hydrolyzed oxysilyl centres at 100.88 eV and 101.62 eV for their and our investigation, respectively. In general, the binding energy of organic Si is close to ~102 eV [49] . The obvious difference stems from the calibrated scale as declared in the experimental, and the difference value (chemical shift) of each peak is just concentrated on here [50, 51].

From the XPS analysis of Si2p and elecrochemical tests, it can be seen that structures of -$Si(OCH_2CH_3)_3$, -$Si(OH)_3$, -$SiO(OH)_2$, and -$SiO_2(OH)$ should be detected during the process. The derivatives or the intermediate products, from the equilibrium between hydrolysis and condensation in the TESPA solution, would become too complex to extract the information of the structures, thus is simply dealt with. The results of Si2p are consistent with the conclusion drawn from the O1s study. The XPS analyses of the individual elements not only reveal the structures of TESPA and TESPA polymeric nanofilm, the chemical reactions between TESPA and copper, as well as the structural changes when the TESPA-treated substrates are heated; but also confirm the protective structures of -SS- units, SiOSi networks, and Cu(I)S complexes. In brief, triazinedithiolsilane compounds incorporate the advantages of triazinedithiol and silane compounds, and hold inherent superiorities over conventional treatments such as phosphating and chromating. These advantages include simple application process, environmental compliance, and excellent corrosion protection of copper, which expedites triazinedithiolsilane compounds as a kind of promising inhibitor for copper.

3.5. Scanning electron microscopy (SEM) and energy dispersive X-ray spectroscopy (EDS)

In order to entirely understand the surface morphology and microstructure of the investigated surfaces, scanning electron microscopy was performed with different scanning scales. Fig. 11 and 12 illustrate the SEM micrographs of 5 μm and 1μm for the bare copper (a), the TESPA-treated copper (b), the hydrolyzed TESPA-treated copper (c), and the hydrolyzed TESPA-treated copper along with following heating (d), respectively. Furthermore, the SEM images of TESPA SAM (e) and polymeric TESPA SAM (f) are also added to compare the morphological difference of the surfaces fabricated by electrochemical and self-assembled techniques. It should be pointed that the concentration of TESPA are identical (5 mM), no matter how the polymeric nanofilms are prepared. Fig. 11a and 12a show the initial surface state of the polished bare substrate. The surface is considerably rough, some fine steaks resulting from the polishing process are visible, and plenty of white spots are obvious which originate from exposed copper. As TESPA is deposited on the bare substrate, some of the white spots disappear

because the exposed copper is coved with TESPA monomers. Nevertheless, some black spots emerge as a result of the electrochemical damage to copper, because some bubbles are observed on the working electrode during the preparation process. This phenomenon reveals that the current density and duration time of galvanostatic method should be adjusted to reduce the damage to copper substrate. In addition, the steaks become obscurer (Fig. 11b) and seem to be filled (Fig. 12b) owing to the coverage of polymeric TESPA nanofilm. The hydrolyzed TESPA-deposited copper surface (see Fig. 11c) is totally different from the former two, the surface of TESPA SAM (Fig. 11e), and the polymeric TESPA SAM (Fig. 11f). The black spots disappear, and the substrate seems to be covered by another type of film which is rougher. The enlarged view with 1μm from Fig. 12c displays that some pores and cracks appear. These changes powerfully demonstrate that a new interface has developed that originates from the hydrolysis of silane part in TESPA. No apparent changes can be observed when the Cu-TESPA-Hydrolysis is heated, i.e., the surface is till rougher and inhomogeneously covered, as shown in Fig. 11d. However, a little difference that the cracks are distributed more uniformly can be seen from Fig. 12d, indicating the SiOH groups atop the Cu-TESPA-Hydrolysis surface condense.

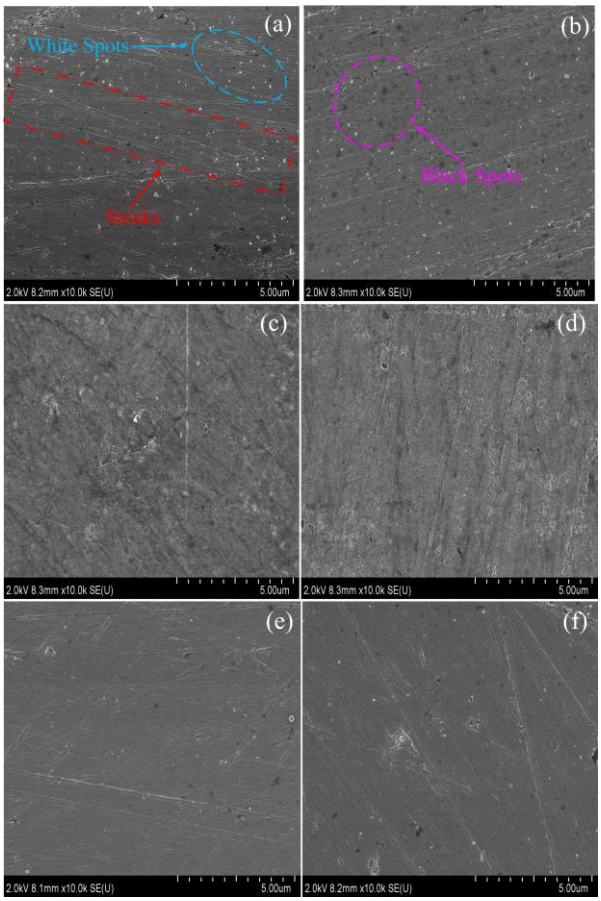

Figure 11. SEM micrographs of the (a) bare copper, (b) TESPA-deposited copper, (c) the hydrolyzed TESPA-deposited copper, (d) the hydrolyzed TESPA-deposited copper plus the following heating under vacuum, (e) self-assembled TESPA on copper, and (f) the heated self-assembled TESPA on copper with 5 μm.

As is shown in our previous work, TESPA monomers are pre-hydrolyzed before reacting with/self-assembling onto copper surface; on the contrary, TESPA monomers are hydrolyzed after reacting with/electrochemically depositing on copper surface. The diverse preparation processes give rise to polymeric nanofilms with various morphologies and microstructures (Fig. 12e and Fig. 12f). In short, the hydrolyzed Cu-TESPA surfaces with/without heating can be effortlessly differentiated from the Cu-TESPA and nanofilms obtained from self-assembled method. A new "interface phase" turns out to shape as the origin of multifunctionality.

We carried out the energy dispersive spectroscopy of the each surface in random areas for five times. The results are identical, indicating that the polymerized nanofilms are uniformly distributed on copper surface. Fig. 13 is just one representative of the each examination, and the existing elements as well as their contents are also listed as the inset tables.

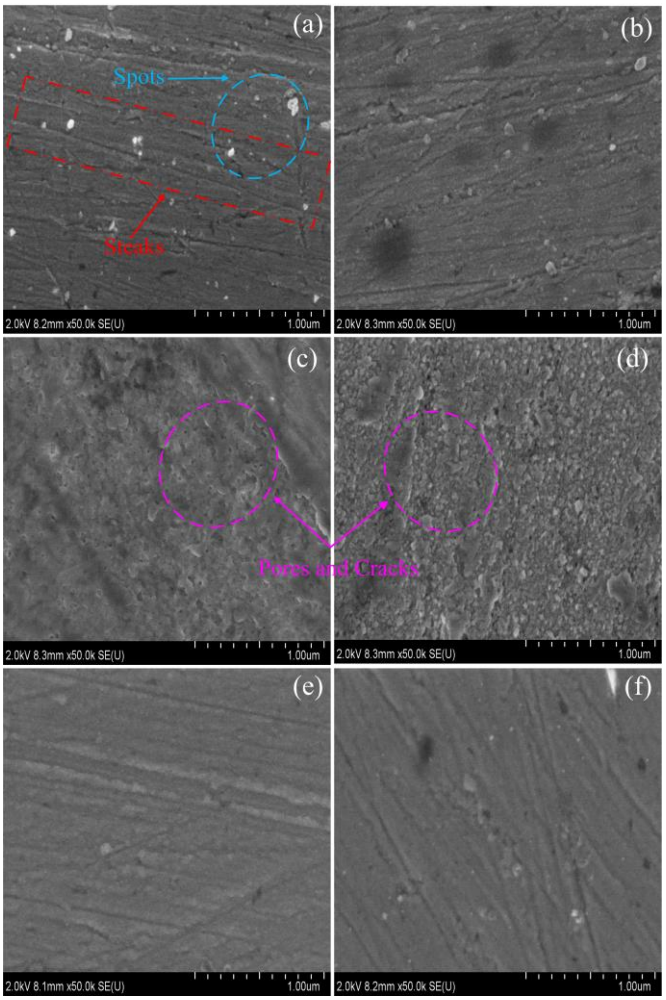

Figure 12. SEM micrographs of the (a) bare copper, (b) TESPA-deposited copper, (c) the hydrolyzed TESPA-deposited copper, (d) the hydrolyzed TESPA-deposited copper plus the following heating under vacuum, (e) self-assembled TESPA on copper, and (f) the heated self-assembled TESPA on copper with 1 μm.

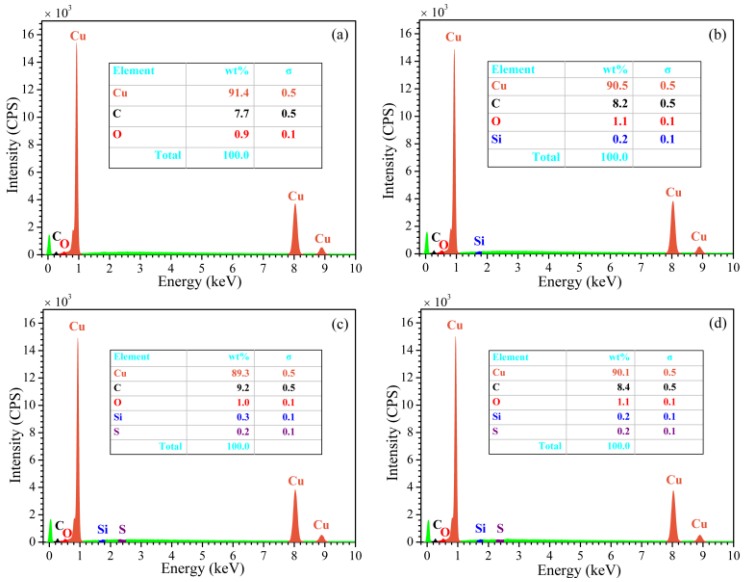

Figure 13. EDS spectra of the (a) bare copper, (b) TESPA-deposited copper, (c) hydrolyzed TESPA-deposited copper, (d) hydrolyzed TESPA-deposited copper plus the following heating under vacuum.

Compared with the reference (Fig. 13a), the TESPA-deposited surface without hydrolysis detects new element of Si (Fig. 13b). For hydrolyzed surfaces with/without heating, both Si and S are observed. From the absence of S and the presence of Si in Cu-TESPA sample, as well as the presence of Si and S in hydrolyzed Cu-TESPA samples, it can be concluded that : (1) When TESPA is electrochemically deposited on copper, by-products yield (also identified by Cu2p and S2p XPS) that surround the -SS- units at the interface between copper and the nanofilm, making sulfur element undetectable by EDS. (2) The by-products can be resolved in acetic acid solution, leading to the re-emergence of sulfur. (3) The directional alignment of TESPA on copper can be confirmed as the contact angle results do, i.e., the silane part in TESPA is located at the top of the nanofilms, and triazinedithiol groups at the bottom, because only Si is observed in Cu-TESPA sample.

4. CONCLUSIONS

Triazinedithiolsilane monosodium salt compounds can be applied to fabricate the multifunctional polymeric nanofilms by electrochemical technique and the following hydrolysis-condensation approach, which are capable of resisting corrosion and activating copper surface concurrently. An important aspect of this work is that the use of XPS to analyze the structural changes of the polymeric nanofilm during the preparation process provides direct evidence for the presence of SCu, SS, and SiOSi at the copper – nanofilm interface. The SEM-EDS results demonstrate that the copper surfaces are uniformly covered with the polymeric nanofilms. When the polymeric nanofilms are hydrolyzed with/without heating, new interface phases develop that are the origins of multifunctionality.

ACKNOWLEDGMENTS
The authors gratefully acknowledge financial supports provided by the National Natural Science Foundation of China (No. 51302280), the Natural Science Foundation of Qinghai (2014-ZJ-936Q), and Young Scholar Project of Qinghai Institute of salt lakes, Chinese Academy of Sciences.

References

1. Y. Wang, Z. Liu, D. Li, Y. Dong, W. Li, N. Li, *Corros. Sci.*, 98 (2015) 382.
2. Y. Wang, Z. Liu, Y. Huang, Y. Qi, *Appl. Surf. Sci.*, 356 (2015) 191.
3. E. Raymundo-Pinero, D. Cazorla-Amoros, A. Linares-Solano, J. Find, U. Wild, R. Schlögl, *Carbon*, 40 (2002)597.
4. Oku, Masaoki, Suzuki, Shigeru, Ohtsu, Naofumi, Shishido, Toetsu, Wagatsuma, Kazuaki, *Appl. Surf. Sci.*, 254 (2008) 5141.
5. M. Alexander, G. Thompson, X. Zhou, G. Beamson, N. Fairley, *Surf. Interface Anal.*, 34 (2002) 485.
6. M. Seah, M. Brown, *J. Electron Spectrosc.*, 95 (1998) 71.
7. C. Perruchot , M. M. Chehimi , M. Delamar , E. Cabet-Deliry , B. Miksa , S. Slomkowski , M. A. Khan , S.P. Armes, *Colloid Polym. Sci.*, 278 (2000) 1139.
8. C. Wagner, L. Davis, M. Zeller, J. Taylor, R. Raymond, L. Gale, *Surf. Interface Anal.*, 3 (1981) 211.
9. P. Swift, *Surf. Interface Anal*., 4 (1982) 47.
10. M. Shi, G. Dunham, M. Gross, G. Graff, P. Martin, *J. Adhes. Sci. Techno.*, 14 (2000) 1485.
11. E.J. Little Jr, M.M. Jones, *J. Chem. Educ.*, 37 (1960) 231.
12. J.-H. Zhou, Z.-J. Sui, J. Zhu, P. Li, D. Chen, Y.-C. Dai, W.-K. Yuan, *Carbon*, 45 (2007) 785.
13. T.I.T. Okpalugo, P. Papakonstantinou, H. Murphy, J. McLaughlin, N.M.D. Brown, *Carbon*, 43 (2005) 153.
14. E. Vassallo, A. Cremona, F. Ghezzi, F. Dellera, L. Laguardia, G. Ambrosone, U. Coscia, *Appl. Surf. Sci.*, 252 (2006) 7993.
15. D. Mitchell, K. Clark, J. Bardwell, W. Lennard, G. Massoumi, I. Mitchell, *Surf. Interface Anal*., 21 (1994) 44.
16. A.O. Lobo, S.C. Ramos, E.F. Antunes, F.R. Marciano, V.J. Trava-Airoldi, E.J. Corat, *Mater. Lett.*, 70 (2012) 89.
17. Y.J. Xu, G. Weinberg, X. Liu, O. Timpe, R. Schlögl, D.S. Su, *Adv. Funct. Mater.*, 18 (2008) 3613.
18. Y. WT, Y. SH, Z. Y, J. J, W. QS, Z. L, J. J., *J. Phys. Chem. B*, 109 (2005) 14011.
19. B. Feng, J. Weng, B. Yang, S. Qu, X. Zhang, *Biomaterials*, 24 (2003) 4663.
20. Q. Xia, B. Wang, Y. Wu, H. Luo, S. Zhao, T. Van Ree, *J. Power Sources*, 180 (2008) 602.
21. K. Kishi, K. Fujiwara, *J. Electron Spectrosc.*, 85 (1997) 123.
22. T. Yano, M. Ebizuka, S. Shibata, M. Yamane, *J. Electron Spectrosc.*, 131 (2003) 133.
23. S. Carniato, F. Rochet, S. Rangan, J.-J. Gallet, G. Dufour, F. Bournel, A. Verdini, L. Floreano, *Phys. Rev. B, Condensed Matter*, 76 (2007) 085321.
24. K.A. Almeida, D. Cardoso, *Catal. Today*, 213 (2013) 122.
25. M. Huang, Y. Zhang, F. Li, Z. Wang, N. Hu, Z. Wen, Q. Liu, *Sci. Rep.*, 4 (2014).
26. M. Yin, C.-K. Wu, Y. Lou, C. Burda, J.T. Koberstein, Y. Zhu, S. O'Brien, *J. Am. Cheml. Soc.*, 127 (2005) 9506.
27. V. Hayez, A. Franquet, A. Hubin, H. Terryn, *Surf. Interface Anal*., 36 (2004) 876.
28. T. Kosec, D.K. Merl, I. Milošev, *Corros. Sci.*, 50 (2008) 1987.
29. P.E. Laibinis, G.M. Whitesides, *J. Am. Cheml. Soc.*, 114 (1992) 9022.
30. K. Mansikkamäki, U. Haapanen, C. Johans, K. Kontturi, M. Valden, *J. Electrochem. Soc.*, 153 (2006) B311.
31. D.G. Castner, K. Hinds, D.W. Grainger, *Langmuir*, 12 (1996) 5083.
32. A.L. Neal, S. Techkarnjanaruk, A. Dohnalkova, D. McCready, B.M. Peyton, G.G. Geesey, *Geochim.*

Cosmochim. Ac., 65 (2001) 223.
33. S. Deng, T. Zhang, Y. Zhang, D. Shan, X. Zhang, *RSC Adv.*, 4 (2014) 29239.
34. K.i. Onisawa, Y. Abe, K. Tamura, T. Nakayama, M. Hanazono, Y.A. Ono, *J. Electrochem. Soc.*, 138 (1991) 599.
35. J.G. Castaño, C. Arroyave, M. Morcillo, *J. Mater. Sci.*, 42 (2007) 9654.
36. T. Ishida, N. Choi, W. Mizutani, H. Tokumoto, I. Kojima, H. Azehara, H. Hokari, U. Akiba, M. Fujihira, *Langmuir*, 15 (1999) 6799.
37. F. Sinapi, S. Julien, D. Auguste, L. Hevesi, J. Delhalle, Z. Mekhalif, *Electrochim. Acta*, 53 (2008) 4228.
38. K. Mori, Y. Oishi, T. Miyashita, M. Matsuda, *Polym. Int.*, 28 (1992) 193.
39. K. Heister, D. Allara, K. Bahnck, S. Frey, M. Zharnikov, M. Grunze, *Langmuir*, 15 (1999) 5440.
40. S. Baskar, C.-W. Liao, J.-L. Chang, J.-M. Zen, *Electrochim. Acta*, 88 (2013) 1.
41. J. Díaz, G. Paolicelli, S. Ferrer, F. Comin, *Phys. Rev. B*, 54 (1996) 8064.
42. Y. Wang, C. Pittman Jr, S. Saebo, *J. Org. Chem.*, 58 (1993) 3085.
43. T. Ward, J. Weber, *Spectrochim. Acta A*, 25 (1969) 1167.
44. A. Pross, L. Radom, R.W. Taft, *J. Org. Chem.*, 45 (1980) 818-826.
45. S.H. Marcus, W. Reynolds, S.I. Miller, *J. Org. Chem.*, 31 (1966) 1872.
46. Z. Xu, S. Lau, P.W. Bohn, *Surf. Sci.*, 296 (1993) 57.
47. R. Socha, K. Laajalehto, P. Nowak, *Surf. Interface Anal.*, 34 (2002) 413.
48. Y. Wang, Q. Yu, Y. Zhang, Z. Guo, N. Gu, K.-D. Wesche, *Appl. Surf. Sci.*, 229 (2004) 377.
49. P.C. Ma, J.-K. Kim, B.Z. Tang, *Carbon*, 44 (2006) 3232.
50. V.P. Zakaznova-Herzog, H.W. Nesbitt, G.M. Bancroft, J.S. Tse, *Surf. Sci.*, 600 (2006) 3175.
51. A. Tiwari, L. Hihara, *Prog. Org. Coat.*, 69 (2010) 16.